AGU PUBLICATIONS

Tectonics

RESEARCH ARTICLE
10.1002/2017TC004648

Key Points:
- Deformed terraces document recent activity of the Minle-Damaying Fault, a structure previously proposed to be inactive during the Holocene
- Vertical slip rates of the fault averaged over the last 12.7 kyr are on the order of 1 mm/yr
- Distribution of active deformation across the eastern Qilian Shan foreland is different to the western and central foreland

Correspondence to:
H. Lu,
hhlv@geo.ecnu.edu.cn

Citation:
Xiong, J., Li, Y., Zhong, Y., Lu, H., Lei, J., Xin, W., … Zhang, P. (2017). Latest Pleistocene to Holocene thrusting recorded by a flight of strath terraces in the eastern Qilian Shan, NE Tibetan Plateau. *Tectonics*, *36*, 2973–2986. https://doi.org/10.1002/2017TC004648

Received 4 MAY 2017
Accepted 8 NOV 2017
Accepted article online 22 NOV 2017
Published online 13 DEC 2017

Latest Pleistocene to Holocene Thrusting Recorded by a Flight of Strath Terraces in the Eastern Qilian Shan, NE Tibetan Plateau

Jianguo Xiong[1,2], Youli Li[2], Yuezhi Zhong[2], Honghua Lu[3], Jinghao Lei[2], Weilin Xin[2], Libo Wang[2], Xiu Hu[2], and Peizhen Zhang[1,4]

[1]School of Earth Sciences and Engineering, Sun Yat-Sen University, Guangzhou, China, [2]Key Laboratory of Earth Surface Processes, Ministry of Education, Peking University, Beijing, China, [3]Key Laboratory of Geographic Information Science of Ministry of Education, School of Geographic Sciences, East China Normal University, Shanghai, China, [4]Institute of Geology, China Earthquake Administration, Beijing, China

Abstract At the eastern Qilian Shan mountain front in the NE Tibetan Plateau, the Minle-Damaying Fault (MDF), the southernmost fault of the North Frontal Thrust (NFT) system, has previously been proposed as an inactive structure during the Holocene. Here we present a detailed record of six strath terraces of the Xie River that document the history of active deformation of the MDF. One optically stimulated luminescence dating sample constrains abandonment of the highest terrace T_6 at 12.7 ± 1.4 ka. The formation ages of the lower terraces (T_4–T_1) are dated by AMS ^{14}C dating. The cumulative vertical offsets of the MDF recorded by these terraces are determined as 12.2 ± 0.4 m (T_6), 8.0 ± 0.4 m (T_5), 6.4 ± 0.4 m (T_4), 4.6 ± 0.1 m (T_3), and 3.2 ± 0.2 m (T_{1c}) by an unmanned aerial vehicle system, respectively. A long-term vertical slip rate of the MDF of 0.9 ± 0.2 mm/yr is then estimated from the above data of terrace age and vertical offset by a linear regression. Assuming that the fault dip of 35 ± 5° measured at the surface is representative for the depth-averaged fault dip, horizontal shortening rates of 0.83–1.91 mm/yr are inferred for the MDF. Our new data show that the proximal fault (the MDF) of the NFT system at the eastern Qilian Shan mountain front has remained active when the deformation propagated basinward, a different scenario from that observed at both the western and central Qilian Shan mountain front.

1. Introduction

Since the Early Cenozoic, the India-Eurasia collision has exerted a major control on the tectonic and topographic development of the Asian inland (Figure 1a) (e.g., Avouac & Tapponnier, 1993; Najman et al., 2001; Tapponnier et al., 2001; Zhang et al., 2004). A striking result of the collision is the growth of the Tibetan Plateau that today reaches average elevations of >4 km. The progressive outward growth of the plateau has caused propagation of thrusting and folding into its surrounding sedimentary basins that accommodate Cenozoic crustal shortening (e.g., Burchfiel et al., 1999; Heermance et al., 2008; Molnar & Tapponnier, 1975; Sobel et al., 2006; Tapponnier et al., 2001; Thompson et al., 2015). The Qilian Shan (Shan means "mountains" in Chinese) on the northeastern margin of the plateau is one of the major ranges that formed over the past ~10 Myr in response to the outward growth of the plateau (e.g., Tapponnier et al., 1990, 2001; Wang et al., 2016; Zheng, Zhang, Ge, et al., 2013; Zheng, Zhang, Zhang, et al., 2013). The history of uplift and growth of the Qilian Shan is thus crucial to understand the process and the mechanism of upward and outward growth of the Tibetan Plateau (e.g., Hetzel et al., 2004, 2006; Pan et al., 2013; Tapponnier et al., 1990; Zheng et al., 2017; Zheng, Zhang, Ge, et al., 2013; Zheng, Zhang, Zhang, et al., 2013).

The Qilian Shan is located in the northeastern margin of the Tibetan Plateau, which comprises several WNW trending mountain ranges (Figure 1a). The crustal shortening of the range is mainly linked kinematically to thrusting of several NW trending reverse faults (Tapponnier et al., 1990; Zhang et al., 2004). Separating the Qilian Shan to the south from the sedimentary basins of the Hexi Corridor to the north, these structures define the steep mountain front of the range (Figure 1a). Previous studies have utilized low-temperature thermochronology (e.g., George et al., 2001), sedimentology and magnetostratigraphy (e.g., Fang et al., 2005; Wang et al., 2016; Zheng et al., 2017), geological and geodetic investigations (e.g., Zhang et al., 2004), or dating of deformed geomorphic surfaces using exposure and luminescence dating (e.g., Hetzel et al., 2004, 2006; Hu et al., 2015; Pan et al., 2013) to constrain the timing and magnitude of the Cenozoic deformation along the

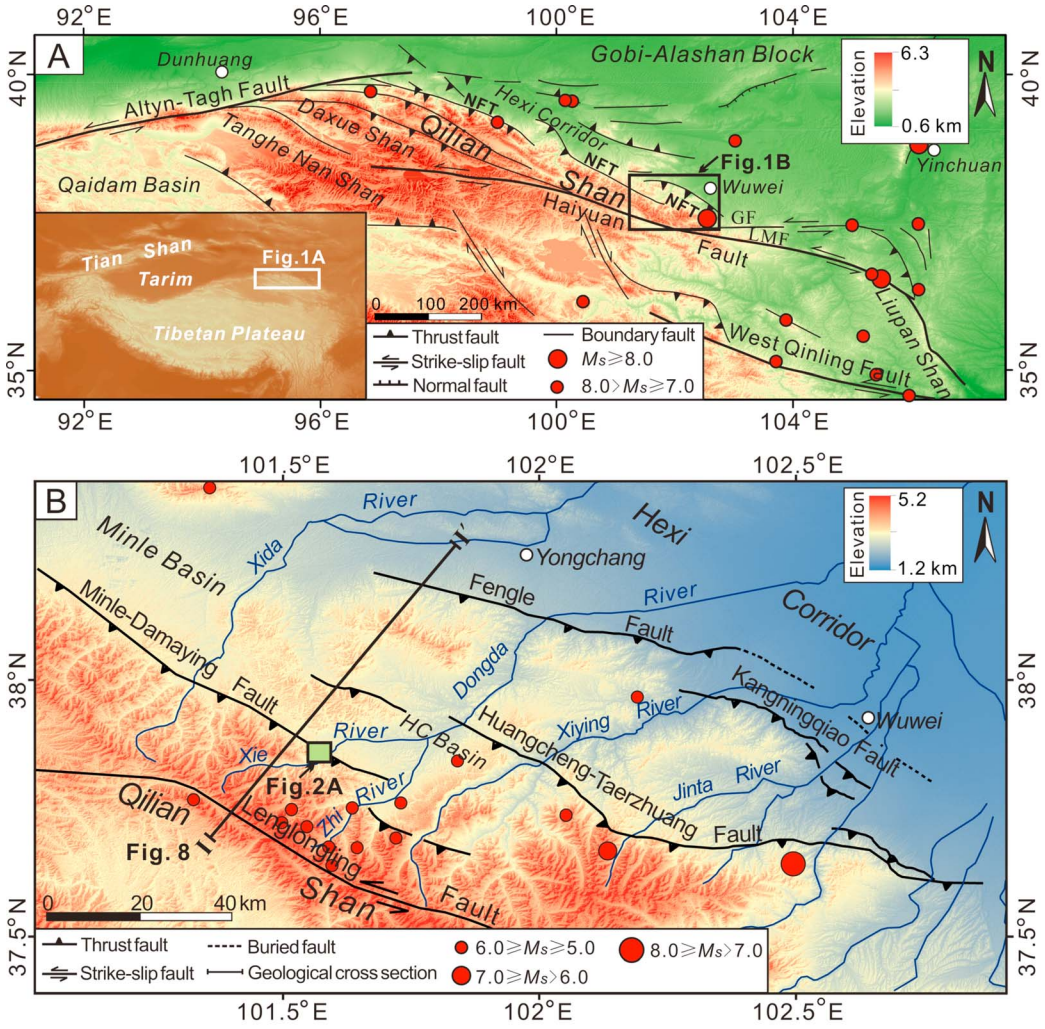

Figure 1. (a) Active tectonics in the northeastern Tibetan Plateau and adjacent regions (Yuan, 2003; Zheng, Zhang, Zhang, et al., 2013) based on a digital elevation model. Insert map showing topography of the Asian Inland. Boundary fault means fault with unknown kinematics. NFT: the north frontal thrust system, GF: Gulang Fault, and LMF: Laohushan-Maomaoshan Fault. (b) Active faults and river systems along the eastern Qilian Shan mountain front. HC Basin: Huangcheng Basin. See Figure 1a for the location of Figure 1b. The earthquake data (since the year AD 1917) are downloaded from the website of USGS: https://earthquake.usgs.gov/earthquakes.

Qilian Shan. Nonetheless, the detailed depositional and geomorphic responses to the ongoing growth of the Qilian Shan still need to be further understood.

Along the margins of active orogenic belts, detailed sedimentological and geomorphological investigations are necessary to understand the tectonic evolution of mountain belts (e.g., Burchfiel et al., 1999; Lavé & Avouac, 2000; Li et al., 1999; Li & Yang, 1998; Lu et al., 2010, 2015, 2017; Molnar et al., 1994; Thompson et al., 2015). In particular, deformed river terraces are very useful in reconstructing the history of active deformation and understanding the kinematics of active structures. Two prerequisites exist when utilizing river terrace to constrain the history of active deformation. One is to establish a robust chronology for terrace formation and/or abandonment, and the other is to precisely determine the magnitude of deformation (e.g., a vertical offset) recorded by the abandoned terrace tread (e.g., Burbank & Anderson, 2012; Yang & Li, 2011).

Here we present a detailed record of the latest Quaternary fluvial terraces of the Xie River, the upper reach of the Dongda River flowing across the eastern Qilian Shan (Figure 1b); the terraces have been sequentially deformed by thrusting of the Minle-Damaying Fault (MDF), a structure at the eastern Qilian Shan mountain

front that has previously been proposed to be inactive during the Holocene (Figure 1b) (IG, LERI, China Earthquake Administration, 1993). A combination of AMS ^{14}C dating and optically stimulated luminescence (OSL) dating was used to constrain the timing of terrace formation and/or abandonment. An unmanned aerial vehicle (UAV) photogrammetry system was then utilized to generate a digital elevation model (DEM) and determine accurate vertical offsets of the MDF at the Xie River. The main aims of this paper are to (1) reveal the latest Quaternary activity of the MDF (timing, magnitude, and rate) and further to (2) discuss the implications of our results for active deformation at the northeastern margin of the Tibetan Plateau.

2. General Setting and Active Tectonics of the Study Area

2.1. General Setting

The Cenozoic growth of the Qilian Shan is controlled by the northeastward propagation of the Tibetan Plateau. Unconformities between Neogene and Jurassic sedimentary rocks (GGB, 1989) indicate that major tectonic deformation occurred during Late Mesozoic or Early Cenozoic. Late Cenozoic deformation along the Qilian Shan range has been controlled by a thrust system that defines the basin-mountain boundary (Gaudemer et al., 1995; IG, LERI, China Earthquake Administration, 1993). In the eastern Qilian Shan between the Xida River and the Xiying River (Figure 1b), ranges comprise mainly Paleozoic and Mesozoic low-grade metamorphic and sedimentary rocks, Late Cenozoic sedimentary strata, and Caledonian granite. Thrusting on the faults at the mountain front places Paleozoic and Mesozoic rocks above Late Cenozoic sedimentary strata (GGB, 1989; IG, LERI, China Earthquake Administration, 1993). In the drainage basin of the Xie River (Figure 1b), the major rock types include Devonian conglomerate and sandstone as well as Lower Carboniferous conglomerate, sandstone, and shale. A small amount of Lower Silurian sedimentary rocks and Lower Ordovician volcanic and metamorphic rocks are found in the upper reach of the Xie River.

2.2. Active Tectonics Along the Eastern Qilian Shan

Active faults in the eastern Qilian Shan deformation zone comprise the Lenglongling Fault and the North Frontal Thrust (NFT) system that includes several northeast vergent thrust faults, that is, the Minle-Damaying Fault (MDF), Huangcheng-Taerzhuang Fault, Fengle Fault, and Kangningqiao Fault (Figure 1b). Along the mountain crest of the eastern Qilian Shan, the southeast striking Lenglongling Fault is a sinistral strike-slip fault with a vertical component (Figure 1b) (He et al., 2010). The Lenglongling Fault is the western segment of the Haiyuan Fault and bifurcates eastward into the Laohushan-Maomaoshan Fault (LMF) to the southeast and the Gulang Fault (GF) to the east (Figure 1a) (He et al., 2010). This left-lateral strike-slip fault system has been active during the Quaternary and exhibits a high seismicity with a series of major historical Earthquakes (e.g., the Haiyuan M_s 8.7 earthquake of 16 December 1920 and the Menyuan M_s 6.4 earthquake of 26 August 1986) (He et al., 2000, 2010; Lasserre et al., 2002; Zhang et al., 1987). The late Pleistocene rate of sinistral slip on the Lenglongling Fault has been estimated to 4.3 ± 0.7 mm/yr (He et al., 2010).

To the north of the Lenglongling Fault, the NFT system dominates the tectonic and topographic patterns of the eastern Qilian Shan (Figure 1b). The MDF is the southernmost fault in the NFT system, which separates the eastern Qilian Shan to the south from the Minle Basin to the north (Figure 1b). This fault roughly dips southward at an angle varying along the strike (IG, LERI, China Earthquake Administration, 1993). On the west bank of the Xie River, a surface dip of 35 ± 5° of the fault has been measured in the field (Figures 2a–2d). The MDF has previously been proposed to have been inactive during the Holocene (IG, LERI, China Earthquake Administration, 1993). However, in this study we show that a flight of well-developed and deformed latest Quaternary terraces of the Xie River records active thrusting of the MDF over the latest Quaternary (Figure 2c). The Huangcheng-Taerzhuang Fault, to the north of the MDF, has also been active in the Holocene with average vertical slip rates estimated to 0.54–0.8 mm/yr on the eastern segment of the fault (Chen, 2003). At least one major history Earthquake, the Gulang M_s 8 earthquake of 23 May 1927, occurred on this fault (Gaudemer et al., 1995). Between the western Huangcheng-Taerzhuang Fault and the eastern MDF, a zone of the sinistral shear has formed a pull-apart basin, that is, the Huangcheng Basin (Figure 1b). The frontal thrusts of the NFT system, the Fengle Fault, and the Kangningqiao Fault define the basin-mountain boundary near the cities of Yongchang and Wuwei (Figure 1b). The average vertical slip rate of the Fengle Fault has been estimated as 2.8 ± 1.3 mm/yr with a horizontal shortening rate of ~2.5 mm/yr over the past ~30 kyr (Champagnac et al., 2010). Although

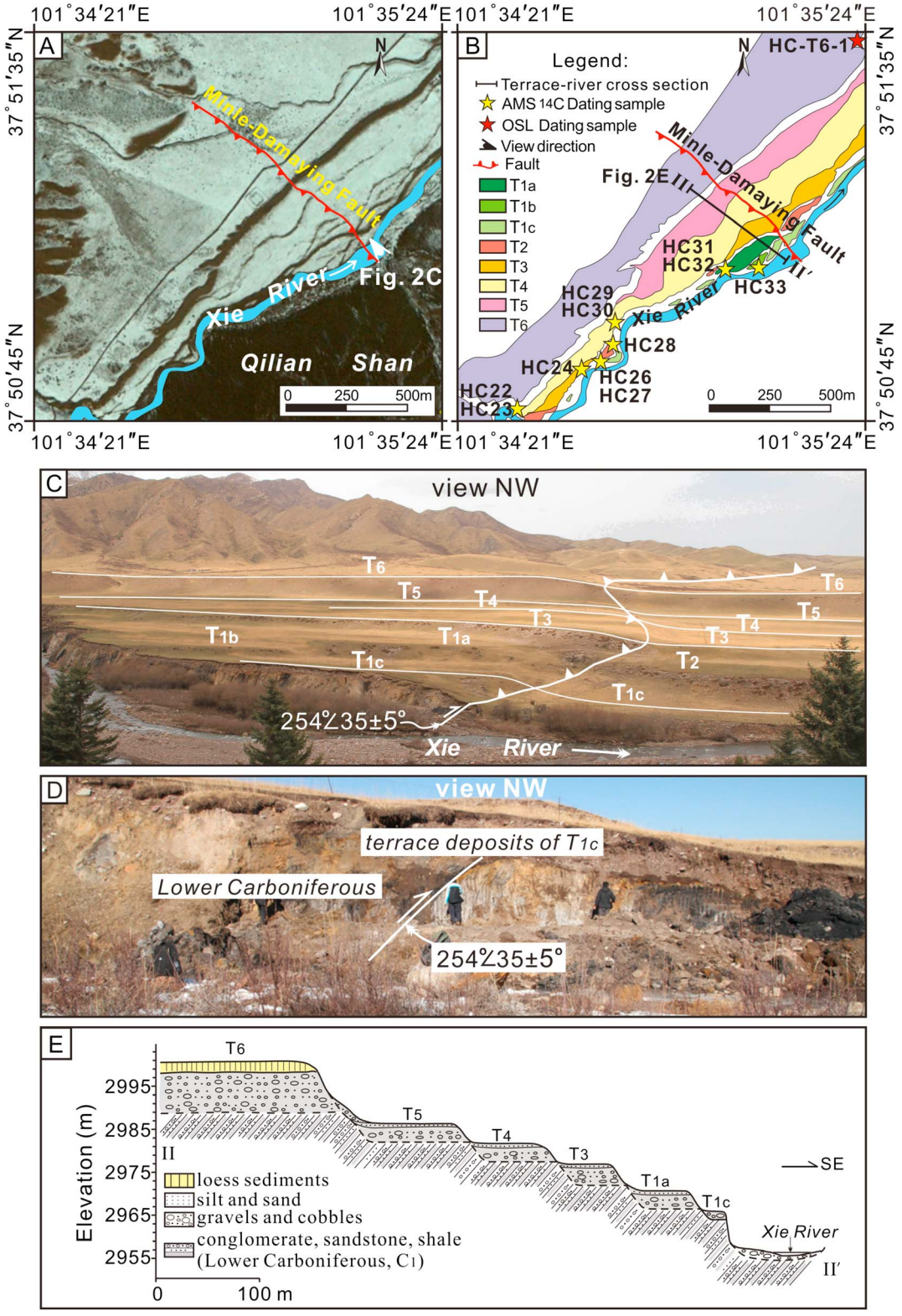

Figure 2. (a) Google Earth image showing the geomorphic framework at the mountain front of the Xie River and (b) the interpreted distribution of the terraces based on detailed field investigations. (c) Photo showing the fault scarps of the Xie River terraces caused by thrusting of the Minle-Damaying Fault. (d) Outcrop of the Minle-Damaying Fault dipping southwestward with an angle of 35 ± 5°. (e) II-II′ terrace-to-river cross section on the hanging wall of the Minle-Damaying Fault showing the geomorphic framework. See Figure 2b for the location of this cross section.

the general framework of the active thrust system at the eastern Qilian Shan mountain front is well characterized (Figure 1b) (IG, LERI, China Earthquake Administration, 1993), the detailed characteristics (timing, magnitude, and rate) of the fault system remain unclear. Until now, no estimate of the Holocene slip rate of the MDF is available. This hinders better understanding of the process and the mechanism of the northeastward growth of the Tibetan Plateau.

3. The Xie River Terraces

3.1. Terrace Classification

Where the Xie River crosses the MDF, we mapped and characterized a flight of six fluvial strath terraces that were deformed above the thrust fault. The geomorphic characterization of terraces in the study area along the Xie River (Figure 2) involved three components. First, fluvial terraces were mapped in the field and using Google Earth images. Second, sedimentology (color, thickness, grain size, roundness, composition, etc.) and geomorphology (height above the modern river and extent of dissection) of the fluvial sediments overlying the bedrock were characterized. Third, based on the mapping, terraces were divided into six levels: T_1 to T_6 increasing systematically in elevation (Figure 2).

All six terraces (T_1–T_6) are beveled into the southwest dipping Lower Carboniferous sandstone and shale, and planated bedrock surfaces (called "strath surfaces") are clearly exposed along the west bank of the river (Figures 2 and 3). The straths are covered with a continuous layer of fluvial deposits that is about 2–4 m thick (for terraces T_1 to T_5) and up to about 7–10 m thick (for terrace T_6) (Figures 2e and 3). Based on these observations, the terraces at the mountain front of the Xie River are defined as strath terraces. The distribution of the low terraces T_1 and T_2 is relatively restricted (Figures 2a and 2b). Terrace T_1 is subdivided into three secondary terraces T_{1a}, T_{1b}, and T_{1c} based on the difference in height above riverbed (Figure 2). The higher terraces T_3 to T_6 are widely distributed along the west bank of the river (Figures 2a and 2b). The surfaces of all terraces are relatively planar and continuous (Figures 2a and 2c), and no obvious erosion and dissection was observed in the field. This observation implies a relatively late timing of abandonment of the terrace caused by river incision. In striking contrast with terraces T_1–T_5, the fluvial deposits of terrace T_6 are covered by ~2.1 m thick aeolian loess (Figures 2e and 4). The terraces are mainly composed of subrounded to rounded pebble-to cobble-sized gravels with the largest boulders reaching several decimeters in diameter (Figure 3). The fluvial gravels on all terraces have a similar distribution of clast lithologies and include mainly sedimentary rocks (sandstone and conglomerate) with a small amount of metamorphic rocks.

3.2. Terrace Formation and/or Abandonment Age

3.2.1. AMS ^{14}C Dating

The time of terrace formation for the low terraces T_1 to T_4 was estimated using AMS ^{14}C dating. Charcoal was collected from layers of sand and silt overlying the terrace gravels (Figure 3). A total of 11 AMS ^{14}C dating samples were taken in the field. In order to well constrain the terrace formation ages, four sets of paired samples were collected (Table 1). The pair HC26-27 and the pair HC29-30 were processed each from one single piece of charcoal (Figures 3c and 3g). In contrast, the pairs HC22-23 and HC31-32 were collected from the same outcrop but in different positions (Figures 3a and 3f).

Following standard procedures (Vries & Barendsen, 1954), the complete sample preparation was performed either at the Beta Analytic (five samples) or the Radiocarbon Dating Laboratory of Peking University (six samples) (Table 1). The charcoal of each sample was pretreated using the acid-alkali-acid (AAA) sequence to remove contaminants (Vries & Barendsen, 1954). The sample was first gently crushed and then dispersed in deionized water. It was then washed with hot hydrochloric acid (HCl) to eliminate carbonates followed by an alkali (NaOH) wash to remove secondary organic acids. The alkali wash was followed by a final acid rinse to neutralize the solution before drying. Finally, the processed samples were transformed into graphite following standard procedures (Santos et al., 2004). The AMS radiocarbon measurements of the prepared graphite samples were performed at both the Beta Analytic (five samples) and the AMS Center, School of Physics, Peking University (six samples). Based on the approach of Talma and Vogel (1993), the ^{14}C ages of the samples were determined with Libby's half-life (5,568 years), the Northern Hemisphere ^{14}C calibration curve IntCal13 (Reimer et al., 2013), and OxCal V4.2 (University of Oxford, 2017). Dates are reported as years before present (present = AD 1950).

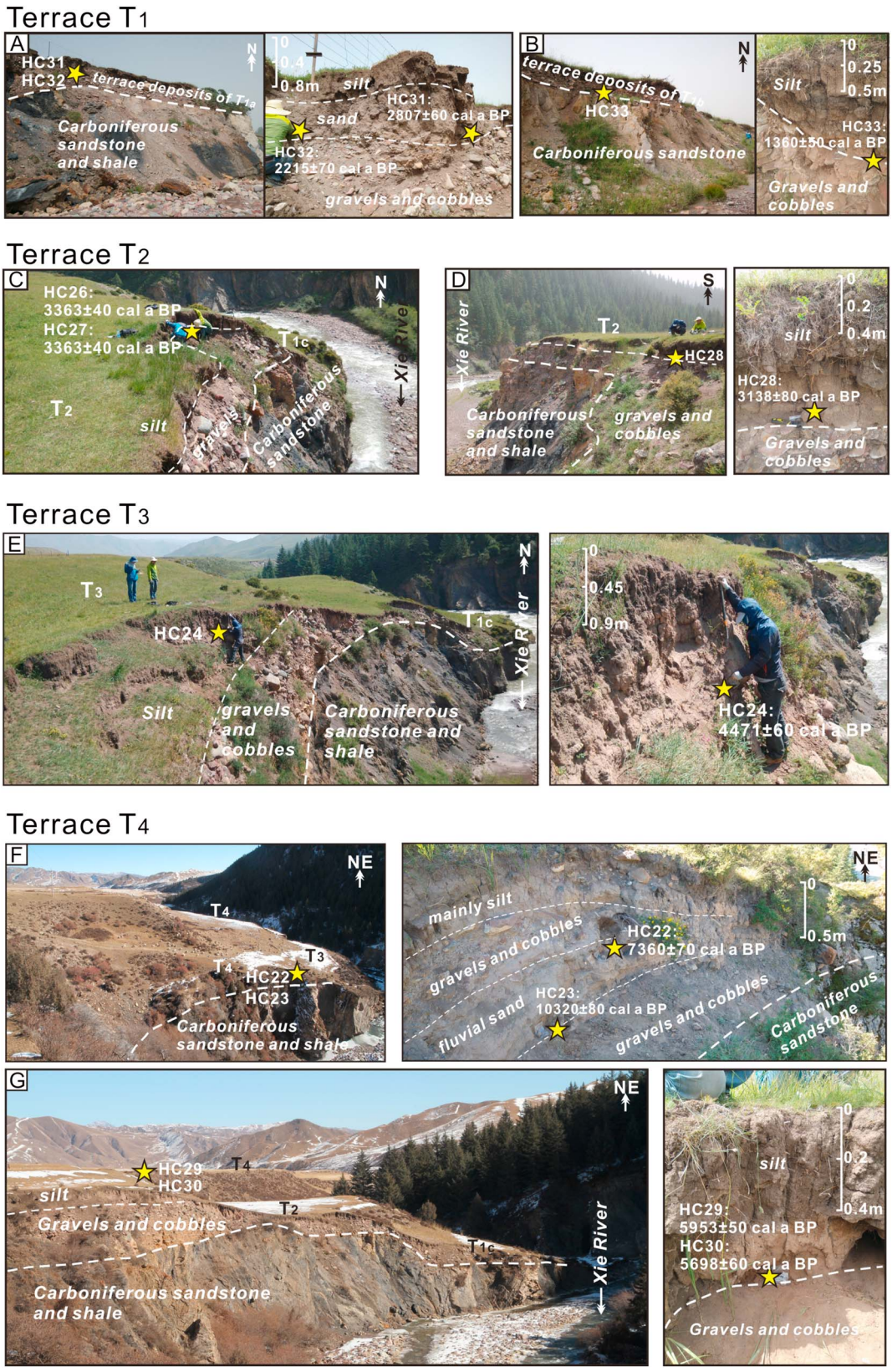

Figure 3. Sampled sections of the AMS ^{14}C dating samples from the terraces T_4–T_1. See Figure 2b for the sampling locations.

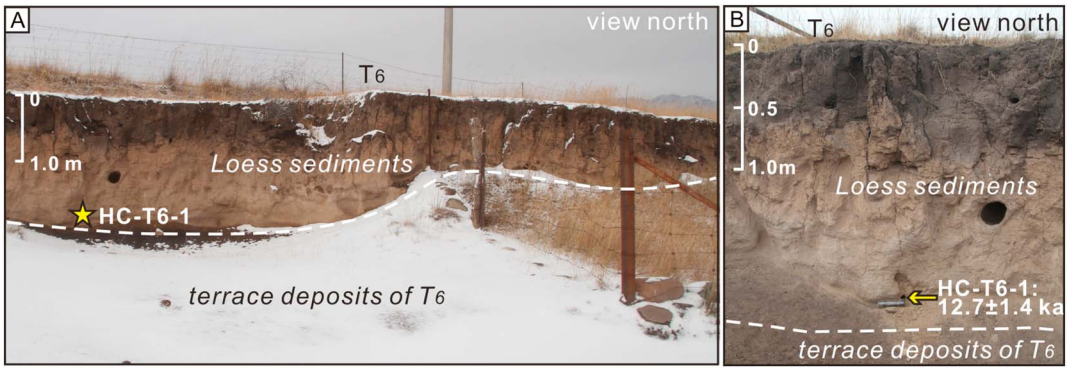

Figure 4. Photograph of ~2.1 thick loess sediments capping the terrace deposits of T_6, from which the OSL sample was taken. See Figure 2b for the location of the sampled section.

3.2.2. Optically Stimulated Luminescence Dating

To estimate the age of the highest terrace T_6 of the Xie River, we took an optically stimulated luminescence (OSL) dating sample from the bottom of the ~2.1 m thick loess sediments capping the fluvial deposits (Figures 2b and 4). Fresh sediments were exposed with a shovel before using a plastic hammer to drive a 20 cm long steel pipe with a diameter of 5 cm into the freshly exposed deposits. The pipe containing the sample remained sealed with opaque materials before processing in the lab.

Following standard procedures (Aitken, 1998), preparation and measurements of the OSL sample were carried out at the OSL Laboratory of the Institute of Geology and Geophysics, Chinese Academy of Sciences. In order to insure maximal shielding, 2–3 cm of the sample was removed from each end of the pipe and only the sample in the center of the steel pipe was analyzed in the lab. About 20 g of loess from the center of the steel pipe were used for water content measurement, and an uncertainty of 10% was assigned. The rest of the loess was first dried and then was treated with 10% hydrochloric acid (HCl) and 10% hydrogen peroxide (H_2O_2) to remove carbonates and organic materials, respectively. Grains $<$90 μm were obtained by mechanical dry sieving, and then were etched with 40% HF for about 80 min to remove feldspar as well as etch the outer alpha dosed layer of quartz grains. Before final rinsing and drying, HCl (10%) was used again to dissolve

Table 1
AMS ^{14}C Dating Data of the Xie River Terraces

Sample no.[a]	Sampled terrace level	Sample location	Terrace elevation at the sampling site (m)[b]	Sampling depth (m)[c]	Conventional ^{14}C age (a BP)	Calibrated ^{14}C cal age (cal a BP)[d]	Terrace formation age (cal a BP)
HC22	T_4	37°50′47.00″N	3005 ± 5	0.60	6445 ± 35	7360 ± 70	5825 ± 130
HC23*		101°34′28.10″E	3005 ± 5	0.90	9160 ± 30	10320 ± 80	
HC29		37°50′57.38″N	2984 ± 5	0.54	5200 ± 30	5953 ± 50	
HC30*		101°34′44.60″E	2984 ± 5	0.68	4980 ± 30	5698 ± 60	
HC24	T_3	37°50′52.70″N	2992 ± 5	0.7	3995 ± 30	4471 ± 60	4471 ± 60
		101°34′39.52″E					
HC26	T_2	37°50′53.25″N	2985 ± 4	0.97	3130 ± 25	3363 ± 40	3288 ± 150
HC27		101°34′42.23″E	2985 ± 4	0.87	3130 ± 25	3363 ± 40	
HC28*		37°50′54.76″N	2982 ± 5	0.97	2970 ± 30	3138 ± 80	
		101°34′44.18″E					
HC31*	T_{1b}	37°51′04.17″N	2969 ± 4	1.16	2710 ± 30	2807 ± 60	2511 ± 300
HC32		101°35′03.63″E	2969 ± 4	0.85	2225 ± 25	2215 ± 70	
HC33*	T_{1b}	37°51′06.01″N	2962 ± 4	0.60	1480 ± 30	1360 ± 50	1360 ± 50
		101°35′11.08″E					

Note. The AMS ^{14}C dating procedure is performed at the Beta Analytic (for the samples marked by the asterisk) and the Radiocarbon Dating Laboratory of Peking University, respectively.
[a]The dating material of all the samples is charred material, and the pretreatment on all the samples is acid/alkali/acid. The sampling locations and the sampled sections are shown in Figures 2b and 3, respectively. [b]The terrace elevation was obtained by a Garmin handheld GPS. [c]The sampling depth was measured by a tape with the scale of 1 cm. [d]Based on the IntCal13 database (Reimer et al., 2013), a simplified approach (Talma & Vogel, 1993) is used to calibrate ^{14}C dates. Reported ^{14}C ages used Libby's half-life (5,568 years) and were referenced to the year AD 1950. The age uncertainty is two sigma.

Table 2
Calculated Values of Equivalent Doses, Annual Doses, and OSL Ages

Sample no.	Sample location	Sampled layer (m)	U[a] (ppm)	Th (ppm)	K (%)	Water content (%) [b]	Equivalent doses (Gy)	Annual doses (Gy/kyr)	OSL age (ka)[c]
HC-T6-1[d]	37°51′35.03″ N 101°35′28.9″ E	The lower part of ~2.1 m thick loess capping the terrace gravels of T_6	3.81	15.6	1.88	6.1	49.7 ± 1.7	3.90 ± 0.17	12.7 ± 1.4

[a]The contents of U, Th, and K were determined using an ELEMENT Plasma Mass Spectrometer. The uncertainty of 5% was taken. [b]An uncertainty of 10% is assigned to the water content. [c]The age uncertainty is two sigma. [d]Location of the dating sample and the sampled terrace cross section are shown in Figures 2b and 4, respectively.

any residual fluorides after etching. The etched grains were sieved again through a 63 μm mesh and then mounted as a monolayer on 9.8 mm diameter aluminum discs using silicone oil as an adhesive. Grains covered the central ~3 mm diameter portion of each disc, corresponding to several hundreds of grains per aliquot. Luminescence measurements were performed on a Risø TL/OSL DA-15 reader. First, the purity of the samples was tested by measuring the infrared stimulated luminescence (IRSL) and 110°C thermoluminescence (TL) peak that is indicative of feldspar. We used a $^{90}Sr/^{90}Y$ beta source with a dose rate of 0.09 Gy/s for dosing and blue light emitting diodes ($\lambda = 470 \pm 20$ nm) and infrared ($\lambda = 830$ nm) LED units for stimulation. Equivalent dose (*De*) of the quartz was determined by using the Simplified Multiple Aliquot Regenerative-dose (SMAR) procedure (Wang et al., 2006). Signals of initial 0.64 s of stimulation were integrated for growth curve construction after subtracting background (last 5 s). To determine the environmental dose rate, U, Th, and K contents in the samples were measured using an ELEMENT Plasma Mass Spectrometer with a relative measurement error of $<5\%$. The cosmic ray dose rate was estimated according to Prescott and Hutton (1994). The environmental dose rate was determined based on the conversion relation between dose rate of quartz and the contents of U, Th, and K and water content (Aitken, 1998). Finally, OSL date for the measured sample was calculated from the acquired *De* and environmental dose rate.

3.2.3. Determination of Terrace Formation and/or Abandonment Age

Ages for T_1 to T_4 obtained by AMS ^{14}C dating are shown in Table 1. Except for the paired samples HC22-23 that have about 3,000 years of difference in age, the small range of radiocarbon ages of the sample pairs HC29-30 and HC31-32 obtained in two different labs (Table 1) lends confidence in our AMS dating. For the terrace T_4, the paired AMS ^{14}C samples HC22 and HC23 yielded two ages that are not within the uncertainty bounds: 7.36 ± 0.07 ka and 10.32 ± 0.08 ka (Table 1 and Figure 3f), both of which are significantly older than the ages of the paired samples HC29 and HC30 (5.95 ± 0.05 ka and 5.7 ± 0.06 ka) taken from the same terrace (Table 1 and Figure 3g). The scattered and older ages of HC22 and HC23 might be attributed to reworking of older deposits upstream and different sources of charcoal. We thus discarded these two older ages (7.36 ± 0.07 ka and 10.32 ± 0.08 ka) and did not use them to constrain the formation age of terrace T_4. We then calculated mean terrace ages for the sample pairs using the accepted ^{14}C age data of the samples taken from the three terraces T_4, T_2, and T_{1a}, and estimated the formation ages of terraces T_4, T_3, T_2, T_{1a}, and T_{1b} to 5.83 ± 0.13 ka, 4.47 ± 0.06 ka, 3.29 ± 0.15 ka, 2.51 ± 0.3 ka, and 1.36 ± 0.05 ka, respectively (Table 1). The errors assigned to the mean ages include the nominal values of the involved individual (two or three) ages. Provided (1) that the charcoal got transported by the river into the terrace deposits and did not form in situ from organic material and (2) that there are no postdepositional formation processes working on the terrace sediments, such as bioturbation, any of the above radiocarbon ages from the charcoal is a maximum age of the deposition of the sampled terrace sediment horizon. Therefore, the calibrated radiocarbon ages of the sampled charcoal fragments found in the fluvial sediments (Table 1) provide a maximum age for the formation of terraces T_1–T_4.

The OSL sample taken from the bottom of the loess overlying the terrace sediments of T_6 constrains the terrace abandonment to 12.7 ± 1.4 ka (Table 2 and Figure 4). It is reasonable to assume that loess begins to accumulate on the terrace after abandonment of the terrace (e.g., Hu et al., 2015; Lu et al., 2014; Pan et al., 2013). Hence, the age of the basal loess provides a reliable minimum age on the timing of terrace abandonment, and the OSL age of 12.7 ± 1.4 ka may be slightly younger than the actual time of terrace abandonment. No suitable material for OSL or AMS ^{14}C dating was found in the terrace deposits of T_5 and T_{1c}; thus, their formation or abandonment ages remain unconstrained.

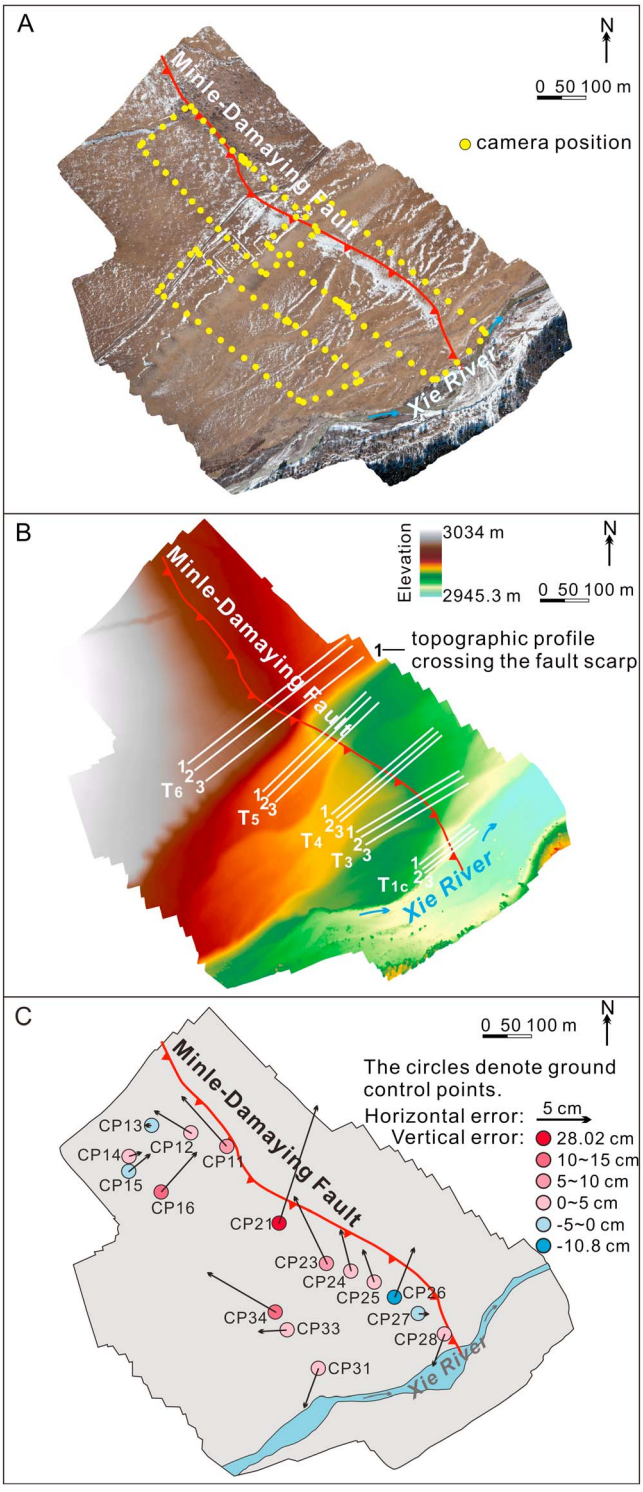

Figure 5. (a) Composite image of the area covering the Minle-Damaying Fault obtained by a DW-01 unmanned aerial vehicle photogrammetry system. Yellow dots show the camera positions ~200 m above the ground. (b) Digital elevation model (DEM) generated from the obtained aerial images using Agisoft PhotoScan. Topographic profiles extracted from the DEM are shown in Figure 6. (c) Sixteen ground control points with associated horizontal and vertical errors which control the resolution of the constructed DEM. The horizontal error of each ground control point is shown as a vector.

4. Vertical Offset of the Minle-Damaying Fault by Morphometry

Photogrammetry acquired by an unmanned aerial vehicle (UAV) system equipped with a camera has progressively become an important tool to obtain landscape surveys. Images obtained by a UAV photogrammetry system can be used to generate a digital elevation model (DEM). In this work, a DW-01 UAV with an octorotor, a Canon EOS 5D Mark II camera, a MX-20 transmitter, a MikroKopter-tool ground controller, and a navigation board was used to obtain areal imagery. Three aerial surveys at an altitude of about 200 m were performed (Figure 5a). In total, 141 images covering an area of 0.51 km^2 were acquired (Figure 5a). The horizontal and vertical precision of the images is about 0.5 m and 0.2 m, respectively. Agisoft PhotoScan was used for photo alignment, dense cloud building, mesh building, and texture building. This standard procedure provided a high-density point cloud to generate a DEM (Figure 5b), and the resolution of the DEM is controlled by 16 ground control points (Figure 5c). The DEM transferred from the obtained aerial images was then used to extract topographic profiles perpendicular to the fault scarp of the MDF (Figures 5b and 6). Finally, the vertical offset of the MDF recorded by each terrace was precisely determined by averaging the offsets of three parallel profiles (Figures 5b and 6). Assuming that erosion and/or sedimentation is zero, the determined vertical offsets recorded by the strath terrace treads can be used to represent the vertical component (rock uplift) of thrusting of the MDF.

The vertical offsets of the fault scarp recorded by the Xie River terraces (Figures 2c and 6) clearly reveal the recent history of thrusting of the MDF. Since terrace T_6 was formed, the cumulative vertical offset of the MDF is 12.2 ± 0.4 m (Figure 6). Both seismic events and/or continuous thrusting of the MDF may have contributed to the total offset since abandonment of terrace T_6. The cumulative vertical offset recorded by the terrace treads decreases sequentially, that is, the younger terrace recording less vertical offset (Figure 6).

5. Estimates of Deformation Rates on the Minle-Damaying Fault

Using the formation ages of the faulted Xie River terraces and the vertical offsets recorded by each terrace tread, the slip rate of the terrace surface above the MDF is calculated, and the uncertainty is estimated based on the uncertainties of the ages and the vertical offsets. First, we calculate the vertical slip rate (vertical component of the fault slip rate) of the MDF by dividing the age of each terrace by the vertical offset of the terrace across the fault scarp. Thus, we obtain a vertical slip rate of 0.96 ± 0.11 mm/yr for T_6. This rate is of the same magnitude as 1.1 ± 0.07 mm/yr recorded by the terrace tread of T_4 and 1.03 ± 0.04 mm/yr recorded by the T_3 terrace tread, respectively. The similarity of vertical slip rates calculated across three different time intervals supports the notion that the MDF had a relatively constant Holocene vertical slip rate over at least the past 12.7 kyr. Finally, we estimate a vertical slip rate of 0.9 ± 0.2 mm/yr from the formation ages of these three terraces and the vertical offsets recorded by their terrace treads by a linear regression using Isoplot (Figure 7). Combined with

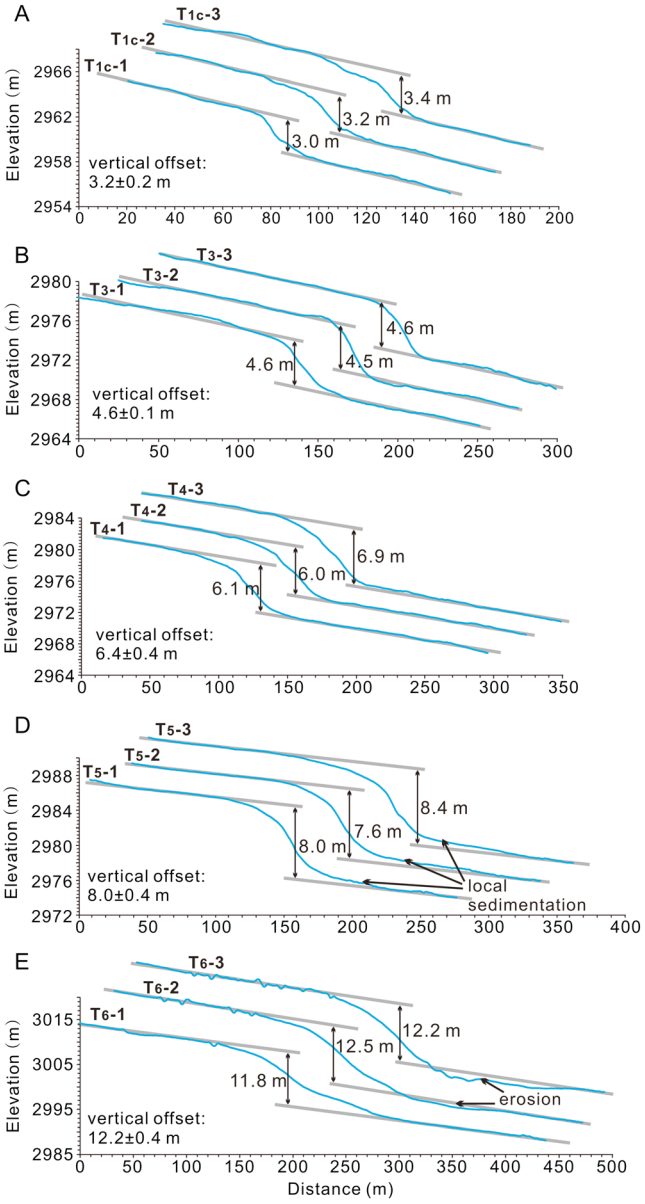

Figure 6. Topographic profiles crossing the fault scarps of the Minle-Damaying Fault. For each terrace, the vertical offset of the Minle-Damaying Fault is estimated by calculating the arithmetic mean of three values based on the three topographic profiles.

the fault dip of 35 ± 5° that was measured on the west bank of the Xie River (Figures 2c and 2d), and provided that the measured surface dip of the fault is representative of the subsurface dip, this vertical slip rate yields an estimated shortening rate (horizontal component of the fault slip rate) of 0.83–1.91 mm/yr on the MDF. As shown in section 3.2.3, the AMS ^{14}C dates on the charcoal fragments from the terrace deposits of T_1–T_4 and the OSL dates on the overlying loess of T_6 provide a maximum and minimum age for the terrace formation and abandonment, respectively. Thus, the obtained rates of vertical slip and shortening for the MDF from these ages would be a little bit underestimated and overestimated, respectively.

6. Discussion

6.1. Implications for Active Deformation Along the Eastern Qilian Shan

Along the eastern Qilian Shan, active deformation is driven mainly by slip on a series of thrust faults. At the mountain front of the Xie River, continuous deformation of the MDF during the latest Quaternary is supported by a flight of successively deformed strath terraces (Figures 2c, 5, and 6). The vertical slip rate over the last 12.7 kyr was estimated as 0.9 ± 0.2 mm/yr (Figure 7), which is of the same order of magnitude as the vertical slip rates of the other reverse faults of the NFT system at the eastern Qilian Shan mountain front (Figures 8 and 9). For example, at the eastern segment of the Huangcheng-Taerzhuang Fault, Chen (2003) has estimated Holocene vertical slip rates to 0.54–0.8 mm/yr by topographic surveying on the fault scarps recorded by river terrace treads and thermoluminescence dating (Figures 8 and 9). Based on AMS ^{14}C dating and paleoseismic trenching, the Holocene vertical slip rate of the Kangningqiao Fault has been estimated as 0.44 ± 0.08 mm/yr (Figures 8 and 9) (Ai et al., 2017). However, there is an exception to these estimates on vertical slip rates. At the eastern segment of the Fengle Fault near the Xiying River (Figures 1b and 9), Champagnac et al. (2010) have estimated the long-term rate of vertical slip of the Fengle Fault as 2.8 ± 1.3 mm/yr over the past ~30 kyr by ^{10}Be exposure dating and topographic surveying. Tectonically, the Kangniangqiao Fault and the Fengle Fault are considered as the eastern and western segments of the Southern Wuwei Basin Fault, respectively (Figures 1b and 9); both of the faults would be expected to have a similar rate of deformation. Relative to the low rate of vertical slip of 0.44 ± 0.08 mm/yr from the Kangningqiao Fault (Ai et al., 2017), however, the rate from the Fengle Fault proposed by Champagnac et al. (2010) is exceptionally high and has been argued to be overestimated due to uncertainties in age control and/or fault offset estimates (Hetzel, 2013; Hu et al., 2015). If the vertical slip rate of 2.8 ± 1.3 mm/yr of Champagnac et al. (2010) is ignored, vertical slip rates are comparable on different faults in the NFT system along the eastern Qilian Shan (Figures 8 and 9).

When combining the estimated vertical slip rates of thrust faults along the eastern Qilian Shan and the measured fault dips at the surface, Chen (2003) has estimated the Holocene rates of horizontal shortening of the Kangniangqiao Fault and the Huangcheng-Taerzhuang Fault as ~0.9 mm/yr and 0.8–1.1 mm/yr, respectively. Recent studies show that distributed folding in response to thrusting on blind faults has accomplished a considerable portion of the deformation (e.g., Hetzel et al., 2006; Hu et al., 2015). For example, in the area between the Huangcheng-Taerzhuang Fault and the Kangningqiao Fault (Figures 1b and 9), formation of the Nanying anticline has resulted from thrusting on such a blind fault with an estimated crustal

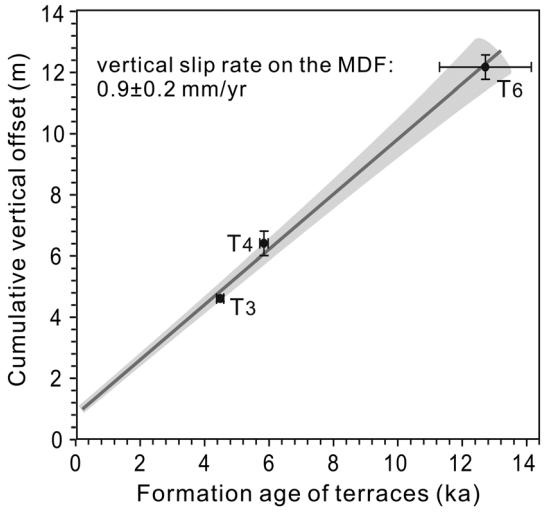

Figure 7. Long-term vertical slip rate of the Minle-Damaying Fault (MDF) estimated from the formation and abandonment ages of the terraces T_6, T_4, and T_3 and the vertical offset recorded by these three terrace treads by a linear regression using Isoplot. The gray shaded envelope displays the uncertainty of the regression. The data of terrace age and vertical offset are from Tables 1 and 2 and Figure 6.

shortening rate of 0.9 ± 0.3 mm/yr (Hu et al., 2015). Together with our estimate of horizontal shortening rate of 0.83–1.91 mm/yr on the MDF, a total of 3–4 mm/yr of crustal shortening inferred from active tectonic studies occurs across the eastern Qilian Shan mountain front. Taking into account the possibility of unrecognized blind thrusts that accommodate the crustal shortening, the actual shortening rate across the eastern Qilian Shan mountain front might be underestimated. On the larger scale, it appears that the cumulative rate of NNE directed shortening across the eastern Qilian Shan mountain front is higher than that along the western Qilian Shan mountain front, where the rate of crustal shortening has estimated to at most ~2 mm/yr (Hetzel et al., 2006).

6.2. Pattern of Active Deformation in the NE Tibetan Plateau

Crustal shortening in the NE Tibetan Plateau has successively encroached into the Hexi Corridor. This outward migration of deformation has resulted in formations of a thrust fault system and fold-and-fault zones (e.g., Li & Yang, 1998; Tapponnier et al., 1990; Zheng et al., 2017; Zheng, Zhang, Ge, et al., 2013; Zheng, Zhang, Zhang, et al., 2013). A series of relatively small mountain ranges have thus developed, such as the Hei Shan, Jintanan Shan, Heli Shan, and Longshou Shan in the northern Hexi Corridor and the Yumu Shan and the Laojunmiao anticline in the southern Hexi Corridor (Figure 9). Based on detailed geologic and geomorphic investigations, the onset of mountain building in the Jintanan Shan and the Heli Shan in the northern side of the Hexi Corridor (Figure 9) has been constrained to ~1.5–1.6 Ma and ~1 to < 3 Ma, respectively (Zheng, Zhang, Ge, et al., 2013; Zheng, Zhang, Zhang, et al., 2013). These ages are younger than the formation age of 3.7 ± 0.9 Ma of the Yumu Shan (Palumbo et al., 2009) as well as the onset of deformation of the Laojunmiao anticline at ~4.9–3.6 Ma (Fang et al., 2005; Zheng et al., 2017) in the southern Hexi Corridor (Figure 9). This difference in age suggests that the deformation front along the northeastern margin of the Tibetan Plateau has reached the northern side of the Hexi Corridor (i.e., the southern Gobi-Alashan Block) since about 2 Ma (Figure 9) (Zheng, Zhang, Ge, et al., 2013).

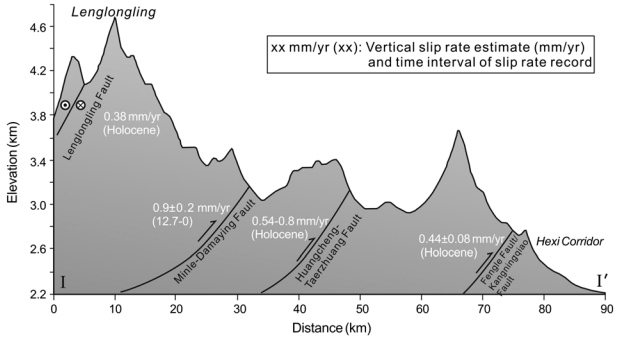

Figure 8. I-I′ cross section with vertical exaggeration. Topography was extracted from the ASTGTM2 DEM with the resolution of 30 m. See Figure 1b for location. The vertical slip rates of the Fengle fault (Kangningqiao Fault), the Huangcheng-Taerzhuang Fault, and the Lenglongling Fault are from Ai et al. (2017), Chen (2003), and He et al. (2000), respectively. All these faults approximately dip southward or southwestward, with dip angles that vary along strike and are commonly estimated to ~40–70° (the Minle-Damaying Fault, IG, LERI, China Earthquake Administration, 1993), ~40–80° (the Huangcheng-Taerzhuang Fault, Chen, 2003), and ~40–90° (the Fengle Fault and the Kangningqiao Fault, Ai et al., 2017).

When the deformation front migrated toward the north-northeast (Zheng et al., 2017), some more proximal (southern) structures in the NFT system at the Qilian Shan mountain front (such as the Red Sand River Fault) have been proposed to become inactive (Hetzel et al., 2004, 2006). Along the western Qilian Shan mountain front, when the deformation propagated northward into the southern Hexi Corridor, the Yumen anticline developing above the Yumen Fault (near the city of Yumen, Figure 9) became active, whereas the proximal basin-mountain boundary thrust became inactive (Hetzel et al., 2006). Along the central Qilian Shan mountain front, a similar history of deformation has been documented, where the proximal Red Sand River Fault became inactive when the Zhangye Fault to the north of the Red Sand River Fault (near the city of Zhangye, Figure 9) was active (Hetzel et al., 2004).

A different scenario is observed at the eastern Qilian Shan mountain front (Figure 9). Our new data show that the proximal fault (here it is the MDF) of the NFT system along the eastern Qilian Shan remains active, even though the distal structures of the NFT system (the Huangcheng-Taerzhuang Fault, the Fengle Fault, and the Kangningqiao Fault, Figures 1b, 8, and 9) are tectonically active during the Holocene (e.g., Ai et al., 2017; Champagnac et al., 2010; Chen, 2003; Hu et al., 2015). A similar pattern of deformation has been documented

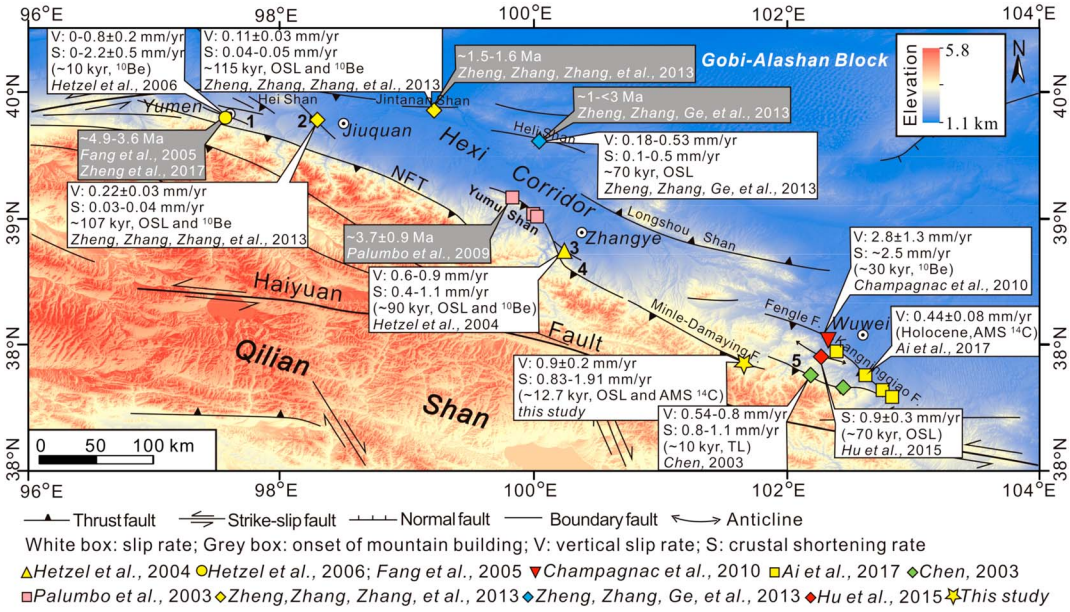

Figure 9. Map showing slip rates on faults (white boxes) as well as constraints on the onset of mountain building (gray boxes) in the southern and northern Hexi Corridor. "(~10 kyr, ^{10}Be)" shows the time interval of slip rate record and the corresponding dating method: ^{10}Be: ^{10}Be exposure dating; AMS ^{14}C: AMS carbon-14 dating; OSL: optically stimulated luminescence dating; TL: thermoluminescence dating. Numbers represent the names of the faults: 1: Yumen Fault; 2: Jiayuguan Fault; 3: Zhangye Fault; 4: Red Sand River Fault; 5: Huangcheng-Taerzhuang Fault.

in the southern Chaiwopu Basin, a piggyback basin in the easternmost part of the northern Chinese Tian Shan foreland (Lu et al., 2015). There, thrusting on the frontal thrust fault, the Banfanggou Fault, in the southern Chaiwopu Basin has driven continuous growth of the Saerqiaoke anticline during the late Quaternary (Lu et al., 2015). In contrast, field observations and measurements on bedding attitudes indicate late Quaternary activity of the proximal Junggar Frontal Thrust Fault (Lu et al., 2015), which separates the northern Chinese Tian Shan range to the south from the Chaiwopu Basin to the north. We propose that the spatial pattern of deformation, as observed along the Qilian Shan mountain front (Hetzel et al., 2004, 2006; this study), could have been driven by the eastward migration of deformation along the NFT system in the NE Tibetan Plateau, but the detailed mechanism behind the spatial pattern of deformation on the NFT is unclear and needs further work.

7. Conclusion

At the mountain front of the eastern Qilian Shan, NE Tibetan Plateau, a flight of six strath terraces document the history of active deformation of the Minle-Damaying fault (MDF), where the fault is cut by the northeastward flowing Xie River. Continuous thrusting of the MDF has faulted six Xie River terraces. Terrace profiles extracted from a high-resolution digital elevation model (DEM) that was obtained by an unmanned aerial vehicle (UAV) system are used to measure the accumulated vertical offset of the MDF. Together with the terrace ages constrained by OSL and AMS ^{14}C dating, we obtain an average vertical slip rate of 0.9 ± 0.2 mm/yr across the past 12.7 ± 1.4 ka. The estimated vertical slip rate of the MDF is comparable with the Pleistocene-Holocene rates from the other thrust faults in the NFT system along the eastern Qilian Shan. Our new data also show that the proximal fault of the NFT system along the eastern Qilian Shan, NE Tibetan Plateau, has remained active when the deformation propagated northeastward into the southern Hexi Corridor.

Acknowledgments
This study is financially supported by the Natural Science Foundation of China (grants 41571001, 41371031, 41590861, and 41661134011), the Special Funds for Earthquake Research from China Earthquake Administration (grant 201408023), and Guangdong Province Introduced Innovative R&D Team of Geological Processes and Natural Disasters (grant 2016ZT06N331). The DEM presented in this paper are uploaded to the Baidu cloud disk (https://pan.baidu.com/s/1hsjEqDe; this link is permanently valid). Gong Zhijun, Zhao Junxiang, and Zhang Jiafu (at Peking University) are especially thanked for their help on the OSL dating and the data analysis. We also thank Yao Yifan and Cheng Lu for their help on the aerial image processing. Zheng Wenjun (at Sun Yat-Sen University) is thanked for thoughtful discussions. Aaron Bufe, one anonymous reviewer, and the Editor Nathan A. Niemi are especially thanked for their constructive comments and language improvements on the earlier version of the manuscript, which resulted in the great improvement of this manuscript.

References

Ai, S., Zhang, B., Fan, C., & Wang, Y. (2017). Surface tracks and slip rate of the fault along the southern margin of the Wuwei Basin in the late Quaternary. *Seismology and Geology*, *39*(2), 408–422. (in Chinese with English abstract).

Aitken, M. J. (1998). *An Introduction to Optical Dating*. Oxford: Oxford University Press.

Avouac, J.-P., & Tapponnier, P. (1993). Kinematic model of active deformation in central Asia. *Geophysical Research Letters*, *20*(10), 895–898. https://doi.org/10.1029/93GL00128

Burbank, D. W., & Anderson, R. S. (2012). *Tectonic Geomorphology* (2nd ed.). Chichester, UK: John Wiley.
Burchfiel, B. C., Brown, E. T., Deng, Q. D., Feng, X., Li, J., Molnar, P., … You, H. (1999). Crustal shortening on the margins of the Tien Shan, Xinjiang, China. *International Geology Review*, *41*(8), 665–700. https://doi.org/10.1080/00206819909465164
Champagnac, J. D., Yuan, D. Y., Ge, W. P., Molnar, P., & Zheng, W. J. (2010). Slip rate at the north-eastern front of the Qilian Shan, China. *Terra Nova*, *22*, 180–187. https://doi.org/10.1111/j.1365-3121.2010.00932.x
Chen, W. B. (2003). Principal features of tectonic deformation and their generation mechanism in the Hexi Corridor and its adjacent regions since late Quaternary. PhD thesis. Institute of Geology, China Seismological Bureau, Beijing, pp. 52–55 (in Chinese).
Fang, X. M., Zhao, Z. J., Li, J. J., Yan, M. D., & Pan, B. T. (2005). Magnetostratigraphy of the late Cenozoic Laojunmiao anticline in the northern Qilian Mountains and its implications for the northern Tibetan Plateau uplift. *Science in China Series D*, *48*, 1040–1051. https://doi.org/10.1360/03yd0188
GGB (1989). *Regional Geology of Gansu Province* (p. 692). Beijing: Geological Publishing House. (in Chinese).
Gaudemer, Y., Tapponnier, P., Meyer, B., Peltzer, G., Shunmin, G., & Chen, Z. T. (1995). Partitioning of crustal slip between linked, active faults in the eastern Qilian Shan, and evidence for a major seismic gap, the "Tianzhu gap", on the western Haiyuan Fault, Gansu (China). *Geophysical Journal International*, *120*(3), 599–645. https://doi.org/10.1111/j.1365-246X.1995.tb01842.x
George, A. D., Marshallsea, S. J., Wyrwoll, K.-H., Chen, J., & Lu, Y. (2001). Miocene cooling in the northern Qilian Shan, northeastern margin of the Tibetan Plateau, revealed by apatite fission-track and vitrinite-reflectance analysis. *Geology*, *29*(10), 939–942. https://doi.org/10.1130/0091-7613(2001)029%3C0939:MCITNQ%3E2.0.CO;2
He, W. G., Liu, B. C., Yuan, D. Y., & Yang, M. (2000). Research on slip rates of the Lenglongling active fault zone. *Northwestern Seismology Journal*, *22*(1), 90–97. (in Chinese with English abstract).
He, W. G., Yuan, D. Y., Ge, W. P., & Luo, H. (2010). Determination of the slip rate of the Lenglongling Fault in the middle and eastern segments of the Qilian Mountain active fault zone. *Earth*, *30*, 131–137. (in Chinese with English abstract).
Heermance, R. V., Chen, J., Burbank, D. W., & Miao, J. (2008). Temporal constraints and pulsed Late Cenozoic deformation during the structural disruption of the active Kashi foreland, northwest China. *Tectonics*, *27*, TC6012. https://doi.org/10.1029/2007TC002226
Hetzel, R. (2013). Active faulting, mountain growth, and erosion at the margins of the Tibetan Plateau constrained by in situ-produced cosmogenic nuclides. *Tectonophysics*, *582*, 1–24. https://doi.org/10.1016/j.tecto.2012.10.027
Hetzel, R., Niedermann, S., Tao, M., Kubik, P. W., & Strecker, M. R. (2006). Climatic versus tectonic control on river incision at the margin of NE Tibet: ^{10}Be exposure dating of river terraces at the mountain front of the Qilian Shan. *Journal of Geophysical Research*, *111*, F03012. https://doi.org/10.1029/2005JF000352
Hetzel, R., Tao, M., Stokes, S., Niedermann, S., Ivy-Ochs, S., Gao, B., … Kubik, P. W. (2004). Late Pleistocene/Holocene slip rate of the Zhangye thrust (Qilian Shan, China) and implications for the active growth of the northeastern Tibetan Plateau. *Tectonics*, *23*, TC6006. https://doi.org/10.1029/2004TC001653
Hu, X. F., Pan, B. T., Kirby, E., Gao, H. S., Hu, Z. B., Cao, B., … Zhang, G. L. (2015). Rates and kinematics of active shortening along the eastern Qilian Shan, China, inferred from deformed fluvial terraces. *Tectonics*, *34*, 2478–2493. https://doi.org/10.1002/2015TC003978
IG, LERI, China Earthquake Administration (1993). *The Qilian Mountain-Hexi Corridor Active Fault System* (p. 340). Beijing: Seismological Press. (in Chinese).
Lasserre, C., Gaudemer, Y., Tapponnier, P., Meriaux, A. S., Van der Woerd, J., Yuan, D. Y., … Caffee, M. W. (2002). Fast late Pleistocene slip rate on the Leng Long Ling segment of the Haiyuan Fault, Qinghai, China. *Journal of Geophysical Research*, *107*(B11), 2276. https://doi.org/10.1029/2000JB000060
Lavé, J., & Avouac, J.-P. (2000). Active folding of fluvial terraces across the Siwaliks Hills, Himalayas of central Nepal. *Journal of Geophysical Research*, *105*(B3), 5735–5770. https://doi.org/10.1029/1999JB900292
Li, Y. L., & Yang, J. C. (1998). Tectonic geomorphology in the Hexi Corridor, north-west China. *Basin Research*, *10*(3), 345–352. https://doi.org/10.1046/j.1365-2117.1998.00070.x
Li, Y. L., Yang, J. C., Tan, L. H., & Duan, F. J. (1999). Impact of tectonics on alluvial landforms in the Hexi Corridor, Northwest China. *Geomorphology*, *28*(3-4), 299–308. https://doi.org/10.1016/S0169-555X(98)00114-7
Lu, H. H., Burbank, D. W., Li, Y. L., & Liu, Y. M. (2010). Late Cenozoic structural and stratigraphic evolution of the northern Chinese Tian Shan foreland. *Basin Research*, *22*, 249–269. https://doi.org/10.1111/j.1365-2117.2009.00412.x
Lu, H. H., Wang, Z., Zhang, T. Q., Zhao, J. X., Zheng, X. M., & Li, Y. L. (2015). Latest Miocene to Quaternary deformation in the southern Chaiwopu Basin, northern Chinese Tian Shan foreland. *Journal of Geophysical Research*, *120*, 8656–8671. https://doi.org/10.1002/2015JB012135
Lu, H. H., Wu, D. Y., Cheng, L., Zhang, T. Q., Xiong, J. G., Zheng, X. M., & Li, Y. L. (2017). Late Quaternary drainage evolution in response to fold growth in the northern Chinese Tian Shan foreland. *Geomorphology*, *299*, 12–23. https://doi.org/10.1016/j.geomorph.2017.09.037
Lu, H. H., Zhang, T. Q., Zhao, J. X., Si, S. P., Wang, H., Chen, S. J., … Li, Y. L. (2014). Late Quaternary alluvial sequence and uplift-driven incision of the Urumqi River in the north front of the Tian Shan, northwestern China. *Geomorphology*, *219*, 141–151. https://doi.org/10.1016/j.geomorph.2014.05.001
Molnar, P., Brown, E. T., Burchfiel, B. C., Deng, Q. D., Feng, X. Y., Li, J., … You, H. C. (1994). Quaternary climate change and the formation of river terraces across growing anticlines on the north flank of the Tianshan, China. *Journal of Geology*, *102*(5), 583–602. https://doi.org/10.1086/629700
Molnar, P., & Tapponnier, P. (1975). Cenozoic tectonics of Asia: Effects of a continental collision. *Science*, *189*(4201), 419–426. https://doi.org/10.1126/science.189.4201.419
Najman, Y., Pringle, M., Godin, L., & Oliver, G. (2001). Dating of the oldest continental sediments from the Himalayan foreland basin. *Nature*, *410*(6825), 194–197. https://doi.org/10.1038/35065577
Palumbo, L., Hetzel, R., Tao, M. X., Li, X. B., & Guo, J. (2009). Deciphering the rate of mountain growth during topographic pre-steady state: An example from the NE margin of the Tibetan Plateau. *Tectonics*, *28*, TC4017. https://doi.org/10.1029/2009TC002455
Pan, B. T., Hu, X. F., Gao, H. S., Hu, Z. B., Cao, B., Geng, H. P., & Li, Q. Y. (2013). Late quaternary river incision rates and rock uplift pattern of the eastern Qilian Shan Mountain, China. *Geomorphology*, *184*(430), 84–97. https://doi.org/10.1016/j.geomorph.2012.11.020
Prescott, J., & Hutton, J. (1994). Cosmic ray contributions to dose rates for luminescence and ESR dating: Large depths and long-term time variations. *Radiation Measurements*, *23*(2-3), 497–500. https://doi.org/10.1016/1350-4487(94)90086-8
Reimer, P. J., Bard, E., Bayliss, A., Beck, J. W., Blackwell, P. G., Ramsey, C. B., … van der Plicht, J. (2013). IntCal13 and Marine13 radiocarbon age calibration curves 0–50,000 years cal BP. *Radiocarbon*, *55*(04), 1869–1887. https://doi.org/10.2458/azu_js_rc.55.16947
Santos, G. M., Southon, J. R., Druffel-Rodriguez, K. C., Griffin, S., & Mazon, M. (2004). Magnesium perchlorate as an alternative water trap in AMS graphite sample preparation: A report on sample preparation at the KCCAMS Facility at the University of California, Irvine. *Radiocarbon*, *46*, 165–173. https://doi.org/10.1017/S0033822200039485

Sobel, E. R., Chen, J., & Heermance, R. V. (2006). Late Oligocene-Early Miocene initiation of shortening in the Southwestern Chinese Tian Shan: Implications for Neogene shortening rate variations. *Earth and Planetary Science Letters*, *247*, 70–81. https://doi.org/10.1016/j.epsl.2006.03.048

Talma, A. S., & Vogel, J. C. (1993). A simplified approach to calibrating ^{14}C dates. *Radiocarbon*, *35*(02), 317–322. https://doi.org/10.1017/S0033822200014077

Tapponnier, P., Meyer, B., Avouac, J.-P., Peltzer, G., Gaudemer, Y., Guo, S., … Dai, H. (1990). Active thrusting and folding in the Qilian Shan, and decoupling between upper crust and mantle in northeastern Tibet. *Earth and Planetary Science Letters*, *97*(3-4), 382–403. https://doi.org/10.1016/0012-821X(90)90053-Z

Tapponnier, P., Xu, Z., Roger, F., Meyer, B., Arnaud, N., Wittlinger, G., & Yang, J. (2001). Oblique stepwise rise and growth of the Tibet Plateau. *Science*, *294*(5547), 1671–1677. https://doi.org/10.1126/science.105978

Thompson, J. A., Burbank, D. W., Li, T., Chen, J., & Bookhagen, B. (2015). Late Miocene northward propagation of the northeast Pamir thrust system, northwest China. *Tectonics*, *34*, 510–534. https://doi.org/10.1002/2014TC003690

University of Oxford (2017). OxCal/ORAU. Retrieved from https://c14.arch.ox.ac.uk/oxcal/OxCal.html

Vries, H. L., & Barendsen, G. W. (1954). Measurements of age by the carbon-14 technique. *Nature*, *174*(4442), 1138–1141. https://doi.org/10.1038/1741138a0

Wang, W. T., Zhang, P. Z., Pang, J. Z., Garzione, C., Zhang, H. P., Liu, C. R., … Yu, J. (2016). The Cenozoic growth of the Qilian Shan in the northeastern Tibetan Plateau: A sedimentary archive from the Jiuxi Basin. *Journal of Geophysical Research*, *121*, 2235–2257. https://doi.org/10.1002/2015JB012689

Wang, X. L., Lu, Y. C., & Zhao, H. (2006). On the performances of the single–aliquot regenerative–dose SAR protocol for Chinese loess–fine quartz and polymineral grains. *Radiation Measurements*, *41*, 1–8. https://doi.org/10.1016/j.radmeas.2005.02.010

Yang, J. C., & Li, Y. L. (2011). *Active Tectonic Geomorphology*. Beijing: Peking University Press. (In Chinese).

Yuan, D. Y. (2003). Tectonic deformation features and space-time evolution in northeastern margin of the Qinghai-Tibetan Plateau since the late Cenozoic time, PhD thesis, Beijing: Institute of Geology, CEA. pp. 106–145 (in Chinese with English abstract).

Zhang, P. Z., Shen, Z., Wang, M., Gan, W., Bürgmann, R., Molnar, P., … You, X. (2004). Continuous deformation of the Tibetan Plateau from global positioning system data. *Geology*, *32*, 809–812. https://doi.org/10.1130/G20554.1

Zhang, W., Jiao, D., Zhang, P. Z., Molnar, P., Burchfield, B. C., Deng, Q., … Song, F. (1987). Displacement along the Haiyuan fault associated with the great 1920 Haiyuan, China, earthquake. *Bulletin of the Seismological Society of America*, *77*(1), 117–131.

Zheng, D. W., Wang, W. T., Wan, J. L., Yuan, D. Y., Liu, C. R., Zheng, W. J., … Zhang, P. Z. (2017). Progressive northward growth of the northern Qilian Shan-Hexi Corridor (northeastern Tibet) during the Cenozoic. *Lithosphere*, *9*(3), 408–416. https://doi.org/10.1130/L587.1

Zheng, W. J., Zhang, H. P., Zhang, P. Z., Molnar, P., Liu, X. W., & Yuan, D. Y. (2013). Late Quaternary slip rates of the thrust faults in western Hexi Corridor (Northern Qilian Shan, China) and their implications for northeastward growth of the Tibetan Plateau. *Geosphere*, *9*(2), 342–354. https://doi.org/10.1130/GES00775.1

Zheng, W. J., Zhang, P. Z., Ge, W. P., Molnar, P., Zhang, H. P., Yuan, D. Y., & Liu, J. H. (2013). Late Quaternary slip rate of the South Heli Shan Fault (northern Hexi Corridor, NW China) and its implications for northeastward growth of the Tibetan Plateau. *Tectonics*, *32*, 271–293. https://doi.org/10.1002/tect.20022